Journal of Materials Chemistry C

ROYAL SOCIETY OF CHEMISTRY

PAPER

View Article Online
View Journal | View Issue



Cite this: J. Mater. Chem. C, 2025, 13, 13803

# $Nb_2CT_x$ MXene integrated $DyMn_2O_5$ composites: tailored particle size and enhanced capacitance for high performance pseudocapacitors†

Komal Ali Rao, *[a] Muhammad Ehsan Mazhar,[a] Javed Ahmad,[a] Muhammad Bilal,[b] Muhammad Imran Khan,[c] Muhammad Suleman Ahmad,[a] Muhammad Aziz[a] and Hafeez ur Rehman[d]

$Nb_2CT_x$, 2D niobium carbide, belongs to the MXene family obtained from $Nb_2AlCT_x$ through selective etching of the Al layer using a non-toxic aqueous KOH solution as an alternative to the hazardous HF etching process. MXene is an emerging material for supercapacitor electrodes due to its distinctive layered structure, large surface area, superior electrical conductivity, and exceptional chemical stability. Owing to the significant energy of the MXene layers, they have a tendency to restack, which limits the effective utilization of the interlayer space for energy storage. Consequently, expanding the interlayer spacing of MXene has become a key research focus to improve its electrochemical performance. Currently, the interlayer spacing of MXene is typically expanded by incorporating nanoparticles. Although numerous bi-metallic transition metal oxides have been explored for this application, only a limited number of rare earth-based bi-metallic oxides have been investigated. Nowadays, the interlayer spacing of MXene is enhanced through the incorporation of nanoparticles. Different bi-metallic transition oxides have been used for this purpose, but very few rare earth-based bi-metallic oxides have been investigated. So in this study, we have synthesized a bi-metallic $DyMn_2O_5/Dy_2O_3$/MXene nanocomposite using a hydrothermal method. X-ray diffraction (XRD) analysis was conducted to determine the crystalline structure and phase purity of the materials. In addition, Fourier-transform infrared spectroscopy (FTIR) and X-ray photoelectron spectroscopy (XPS) were performed to investigate the functional groups, chemical bonding and multiple oxidation states in the composites, respectively, providing further confirmation of successful synthesis. Scanning electron microscopy (SEM) coupled with energy-dispersive X-ray spectroscopy (EDX) was employed to analyze the surface morphology and confirm the cubic-shaped pellet-like nanoparticles on the MXene layers, as well as to verify the elemental composition and uniform distribution of constituent elements. The optimized electrode material demonstrates a marvelous specific capacity of 362.92 C $g^{-1}$ at a current density of 1 A $g^{-1}$, along with excellent cycling stability. An asymmetric supercapacitor is fabricated using the $DyMn_2O_5/Dy_2O_3$/MXene nanocomposite as the anode and activated carbon as the cathode. The assembled device achieves an energy density of 46.25 W h $kg^{-1}$ at a power density of 705 W $kg^{-1}$, retaining 70.56% of its initial capacitance after 10 000 charge discharge cycles at 2 A $g^{-1}$. This study introduces an efficient hydrothermal method for the synthesis of an innovative rare earth and MXene-based nanocomposite with controlled particle size for the electrode of supercapacitors.

Received 28th March 2025,
Accepted 21st May 2025

DOI: 10.1039/d5tc01337b

rsc.li/materials-c



## 1. Introduction

Overpopulation, excessive consumption of renewable energy sources, industrial expansion, and the rapid depletion of fossil fuels have raised significant concerns regarding the global energy crisis. Energy sources that are effective, green, clean, affordable, sustainable and renewable are urgently needed to replace traditional energy sources in order to address these issues. Although there are plenty of natural resources,

[a] Institute of Physics Bahauddin Zakariya University, Multan-60800, Pakistan. E-mail: komalrao49@gmail.com
[b] School of Engineering and Materials Science, Queen Marry University of London-E1 4NS, UK
[c] Research Institute of Sciences and Engineering (RISE), University of Sharjah, Sharjah 27272, United Arab Emirates
[d] Center for Green Innovation, School of Mathematics and Physics, University of Science and Technology Beijing, Beijing, 100083, China

† Electronic supplementary information (ESI) available. See DOI: https://doi.org/10.1039/d5tc01337b

including wind, solar power, thermal, tidal, and hydroelectric, the scientific community still has a difficult time in storing and utilizing them.[1–4] As a result, the need for advanced energy storage and conversion technologies has significantly increased. Many advanced energy storage devices, capacitors, batteries, fuel cells, sensors and super capacitors that store energy electrically and chemically are the major solutions to mitigate energy challenges.[5–9] Batteries and supercapacitors[10] are the most reliable and practical methods of electrochemical energy storage at the interface between a conducting electrode and an electrolyte.[11–15] Supercapacitors have attracted the interest of battery makers due to their ability to reduce the gap between power density and energy density. High energy density while maintaining higher power density are both essential in the field of energy storage and transmission. On the basis of the types of electrode materials and electrochemical process, supercapacitors are commonly divided into two types, electric double layer capacitors (EDLC) and pseudocapacitors.[16] Carbon or activated carbon-based materials are used as electrode materials in the first type and metal oxides/conducting polymers in the second type of supercapacitor.[17,18] However, a significant effort is being made by researchers to find suitable pseudocapacitive materials and methods of production in order to build such storage units. The optimal electrode material for pseudocapacitors (PCs) with superior power and energy densities must satisfy the following stringent criteria: (i) exceptional electrical conductivity, an extensive specific surface area, and enhanced ion transport pathways to facilitate efficient charge storage and rapid electrochemical response; (ii) abundant redox-active sites coupled with ultrafast charge-transfer kinetics to enable high-rate electrochemical reactions and maximize energy storage efficiency.[19–21] Transition metal oxides (TMOs) exhibit exceptional electrochemical properties, characterized by high theoretical capacities and versatile redox activity, making them highly suitable for energy storage applications. However, their practical deployment is constrained by inherent drawbacks such as limited electrical conduction, slow ion diffusion, and structural degradation during cycling. To mitigate these limitations, integrating TMOs with carbon-based materials such as graphene, carbon nanotubes, or activated carbon or novel MXene carbides—has proven to be a highly effective strategy. Sometimes, one metal in binary TMOs can be replaced by a rare earth metal because rare earth metals such as La, Dy, Er, and Ce have multiple valence states, and a high value of conductivity. These conductive matrices enhance charge transport, reduce internal resistance, and provide mechanical stability, thereby counteracting volume fluctuations during charge–discharge processes. This synergistic combination significantly improves electrochemical performance by enhancing specific capacity, rate capability, and cycling stability.[22,23] Composites based on rare earth metal oxides are an example that satisfy those requirements and may be utilized to develop electrode materials with a high energy and power density, where the various valence states of the rare earth metals may be fully used for increased charge storage capacity together with a maximum operating voltage.[24] The two primary chemical processes that rare earth compounds undergo are chemical redox reactions and acid base reactions. Rare earth-based metal oxides are thought to be possible pseudocapacitors because of their redox characteristics and preferred conductivity. In addition, they possess maximum bulk density, which is thought to be particularly beneficial in producing outstanding volumetric capacitance.[25–30] There are a few reports of rare earth metal-based oxides functioning as the electrode of supercapacitors. The specific gravimetric capacitance of rare earth compounds is quite low, ranging from 200 to 300 F $g^{-1}$, compared to other transition metal oxides including nickel oxides, cobalt oxides, and manganese oxides. However, due to their significantly higher density, rare earth compounds have a very high volumetric capacitance.[31–33] As examples, $LaMnO_3$,[34] $SrMnO_3$,[35] $Y_2NiMnO_6$,[36] and $LaCrO_3$[37] electrodes exhibit pseudocapacitance behavior with efficient specific capacitance and remarkable cycling stability. Among these, dysprosium-based manganese oxides ($DyMn_2O_5$) offer intriguing properties due to the synergistic combination of manganese's rich redox chemistry and dysprosium's ability to stabilize the crystal structure and enhance electrical conductivity. While $DyMn_2O_5$ has been studied for its magnetic and structural properties, its electrochemical behavior remains largely unexplored. Pseudocapacitance is produced by the oxygen-containing ions in the electrolyte by manganese oxidation/reduction and direct absorption into the voids of the perovskite structure. Manganese-based metal oxides were shown to be a good substitute because to their favourable electrochemical properties, natural availability, affordability, strong redox activity, eco-friendliness, & substantial potential capacitance.[38–40] Also, to further enhance the conductivity and cycling performance of $DyMn_2O_5$, MXene and other carbon-based materials can be added. MXenes have emerged as highly promising materials in energy storage research due to their advanced two-dimensional framework, rich surface chemistry, excellent mechanical properties, and exceptional electrical conductivity. Their general chemical composition is represented as $M_{n+1}X_nT_x$ where $n$ denotes integer values (*e.g.*, 1, 2, 3), and T corresponds to surface functional groups such as –OH, –O, and –F. Extensive investigations have led to the discovery of more than 20 MXene variants, including $VC_4$, $Ti_2C$, $Nb_2C$, and $Nb_4C_3$, among others.[41–43] These different types of MXene composite with metal oxides are used in energy storage devices and electrochemical sensors also. N. Prabhakar *et al.* studied the $Nb_4C_3T_x$ @WO composite for a high performance asymmetric supercapacitor, delivering a specific capacitance of 1045 F $g^{-1}$ at 1 A $g^1$.[44] Furthermore, P. Varatharjan *et al.* fabricated a sensor system with remarkable selectivity, stability and excellent reproducibility for the sensing of *p*-nitrotoluene using $MnCo_2O_4$@ $Ti_3C_2T_x$.[45] U. Rajaji *et al.* used $MoS_2$/S-$Ti_3C_2$/LGE as an electrochemical sensing medium for the detection of poisonous roxarsone and aristolochic acid.[46] Similarly, MXene base composites with metal oxides *e.g.* Dy-$WO_3$/PCNFs, δ-$MnO_2$@$Ti_3C_2T$, $MnO_2$/MXene, $CoCr_2O_4$@MXene, $ZrO_2$-doped $V_2CT_x$ MXene, cobalt ion-doped $V_2CT_x$ MXene, Ni–$Mn(OH)_2$@$V_2CT_x$,

 

$Mn_3O_4$@MXene, and $Ti_3C_4$@$Mn_3O_4$@carbonized iron, are used as electrode materials of supercapacitors.[47–54] Structurally, MXenes comprise alternating layers of transition metals and carbon, imparting high electrical conductivity. Their characteristic of an accordion-like morphology facilitates the reversible intercalation of ions and molecules, effectively increasing the interlayer spacing and specific surface area, making them ideal candidates for electrochemical energy storage systems. Among various MXene compositions, $Nb_2CT_x$ has been extensively studied due to its layered architecture, enabling its application as an electrode material with outstanding electrochemical properties.[55] However, strong interlayer van der Waals forces lead to significant stacking, reducing the accessible surface area and limiting charge storage efficiency. Consequently, expanding the interlayer spacing and preventing restacking are critical research priorities to enhance MXene's performance in energy storage applications.[56]

Multiple literature have been reported on the preparation of $DyMn_2O_5$ that have looked at their magnetic characteristics and crystal structure.[57] Despite extensive studies on individual pseudocapacitive materials, there is a critical gap in the research regarding the integration of rare earth metal oxides with MXenes for electrochemical energy storage. Based on the available literature, there are no reported studies on the synthesis and electrochemical investigation of $DyMn_2O_5$/MXene ($Nb_2CT_x$) composites. The rational design of these composites leverages the high redox activity of $DyMn_2O_5$ and the exceptional electrical conductivity of $Nb_2CT_x$ MXene, addressing the limitations of both materials. The synergistic effect of these components is expected to enhance the charge transfer kinetics, improve structural stability, and increase overall electrochemical performance.

The selection of $DyMn_2O_5$ and $Dy_2O_3$ among rare earth oxides was based on their synergistic electrochemical and structural characteristics, which are particularly advantageous for energy storage systems. $DyMn_2O_5$, a mixed metal oxide containing transition and rare earth metals, provides multiple accessible oxidation states of manganese, enabling fast and reversible faradaic redox reactions. Dysprosium within this compound also contributes to improved electronic conductivity and stability through its 4f orbitals.[58] Moreover, they possess high bulk density, which significantly contributes to achieving superior specific capacitance. To optimize their combined performance, various compositions were systematically investigated by adjusting the weight or molar ratios.

In this study, $DyMn_2O_5$/MXene ($Nb_2CT_x$) composites were synthesized using a hydrothermal method and evaluated as electrode materials for supercapacitor applications. The incorporation of $Nb_2CT_x$ MXene is anticipated to enhance the conductivity and electrochemical stability of $DyMn_2O_5$, leading to improved power and energy density. This work not only introduces a novel electrode material, but also contributes to the broader field of MXene-based hybrid materials for advanced energy storage technologies.

## 2. Experimental procedure

### 2.1. Materials

Dysprosium(III) nitrate ($Dy(NO_3)_3$, 99% purity), manganese(II) nitrate ($Mn(NO_3)_2$, 99% purity), potassium hydroxide (KOH, 98% purity) and MAX ($Nb_2AlC$, 99% purity) all were obtained from Sigma Aldrich. Deionized water and ethanol (99.9% purity) and no other procedures were required to clean the materials, because all materials used in the experiment were analytical quality.

### 2.2. Synthesis of MXene ($Nb_2CT_x$)

Initially, 0.2 g of $Nb_2AlCT_x$ (MAX phase powder) was dispersed in 1 mL of distilled water in a beaker. In a separate beaker, 2 g of potassium hydroxide (KOH) was dissolved in 2 mL of distilled water under stirring. The prepared KOH solution was then gradually added to the $Nb_2AlCT_x$ dispersion while maintaining continuous stirring. The resulting mixture was transferred to a mortar and pestle and finely ground for 1 hour until a thick paste was formed. This paste was then placed into a stainless steel autoclave and subjected to thermal treatment at 150 °C for 24 hours. After the heating process, the autoclave was removed, and the obtained precipitates were collected and thoroughly washed with ethanol and distilled water multiple times to eliminate any residual impurities. The final product was dried in a vacuum oven at 80 °C for 24 hours, yielding a black colored $Nb_2CT_x$ MXene powder, as shown in Fig. 1.

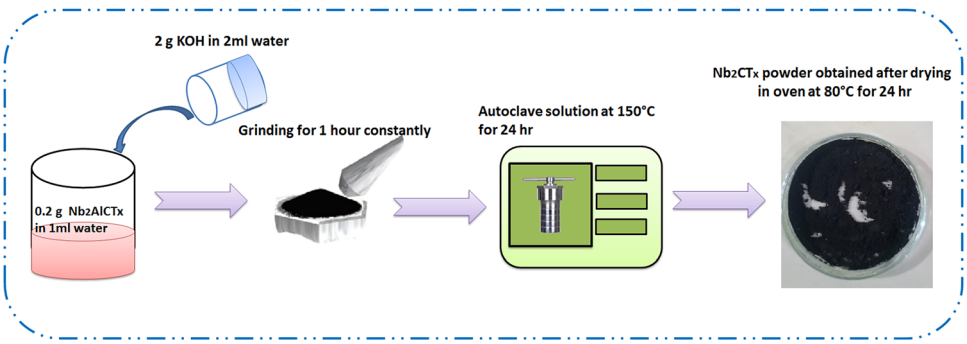


Fig. 1 Schematic illustration of the synthesis of $Nb_2CT_x$ MXene from $Nb_2AlC_2T_x$.

### 2.3. Preparation of $DyMn_2O_5$ $Dy_2O_3$/MXene ($Nb_2CT_x$) and $DyMn_2O_5/Dy_2O_3$ composites

$DyMn_2O_5/Dy_2O_3$/MXene ($Nb_2CT_x$) was synthesized *via* a hydrothermal method. Initially, 1 mmol of dysprosium nitrate ($Dy(NO_3)_3$) and 2 mmol of manganese nitrate ($Mn(NO_3)_2$) were dissolved in 30 mL of distilled water under magnetic stirring for 1 hour. Here, 0.1 g of synthesized MXene ($Nb_2CT_x$) in 5 mL distilled water was added dropwise into the precursor solution under constant stirring. Separately, 2 g of potassium hydroxide (KOH) was dissolved in 20 mL of distilled water, and the resulting solution was gradually added dropwise to the stirred precursor solution until the pH was adjusted to 7–8. The obtained solution was then transferred into a Teflon-lined stainless steel autoclave and subjected to thermal treatment at 180 °C for 12 hours to facilitate solvent evaporation. When the solution in the autoclave was cooled down at room temperature, it was washed multiple times with ethanol and distilled water, and subsequently subjected to centrifugation five times at 4000 rpm for 20 minutes to obtained pure precipitates. The collected precipitates were dried in an oven at 80 °C for 12 h. Finally, a light yellowish powder was obtained and annealed at 750 °C for 6 hours in a furnace to enhance its structural and functional properties. A schematic diagram of the synthesis technique for the preparation of the $DyMn_2O_5/Dy_2O_3$/MXene (DMO/DO/MX) composite is shown in Fig. 2.

For comparison, the $DyMn_2O_5/Dy_2O_3$ (DMO/DO) composite was synthesized by following the same amount of precursors, and the same synthesis protocols as mentioned above without adding MXene ($Nb_2CT_x$) in solution.

### 2.4. Preparation of the electrode

A three-electrode configuration was employed for electrochemical measurements. The system consisted of a reference electrode (Ag/AgCl), a counter electrode (platinum wire), and a working electrode composed of nickel foam coated with $DyMn_2O_5/Dy_2O_3$/MXene ($Nb_2CT_x$). The fabrication of the working electrode involved grinding of 0.1 g of $DyMn_2O_5/Dy_2O_3$/MXene (DMO/DO/MX) powder in a mortar and pestle for approximately one hour to achieve a fine particle dispersion. A few drops of water were then added to form a homogeneous aqueous slurry. The prepared slurry was uniformly applied onto a 1 cm × 1 cm nickel foam substrate, followed by drying in an oven at 75 °C for 12 hours. Using the same procedure, a $DyMn_2O_5/Dy_2O_3$ (DMO/DO) electrode was fabricated. The active loaded mass of $DyMn_2O_5/Dy_2O_3$/MXene and $DyMn_2O_5/Dy_2O_3$ was 2.5 mg and 2.8 mg, respectively.

## 3. Results and discussion

### 3.1. Structural analysis

**3.1.1. XRD analysis.** The crystal structure and phase purity of the synthesized samples were analyzed using X-ray diffraction (XRD). Fig. 3 presents the diffraction patterns that were indexed using X'Pert Highscore software. Fig. 3(a) presents the XRD pattern of the synthesized $Nb_2CT_x$ MXene, where the characteristic diffraction peaks at $2\theta$ = 33.4°, 36.4°, 38.2°, 59.6°, and 72.7° correspond to the (100), (002), (101), (110), and (201) planes, respectively, as indexed to the

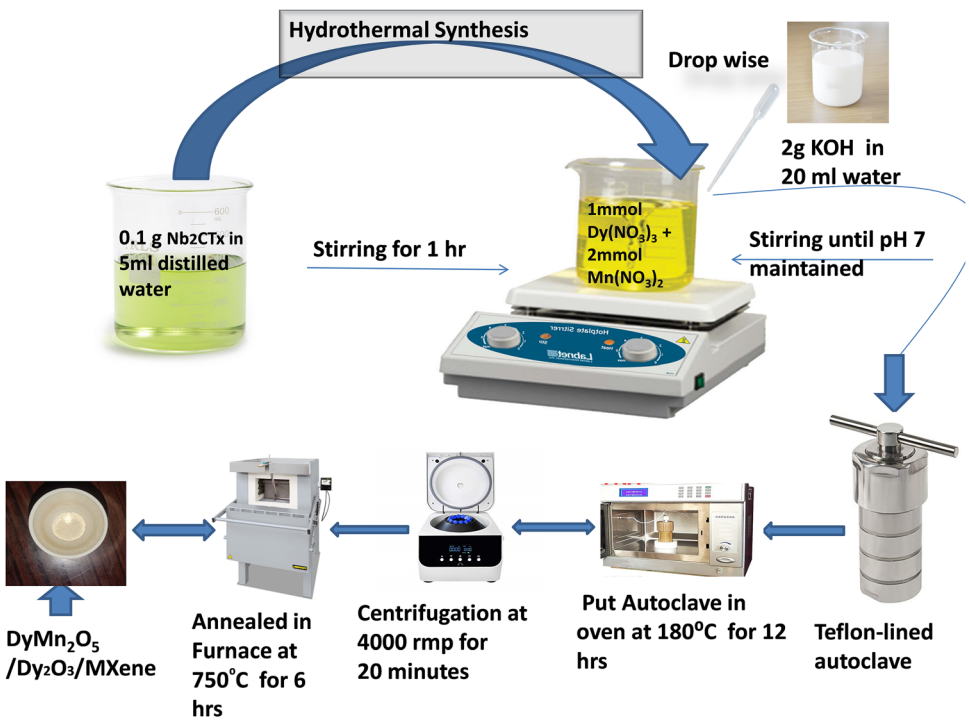


Fig. 2 Hydrothermal synthesis of nanocomposite $DyMn_2O_5/Dy_2O_3$/MXene.

 

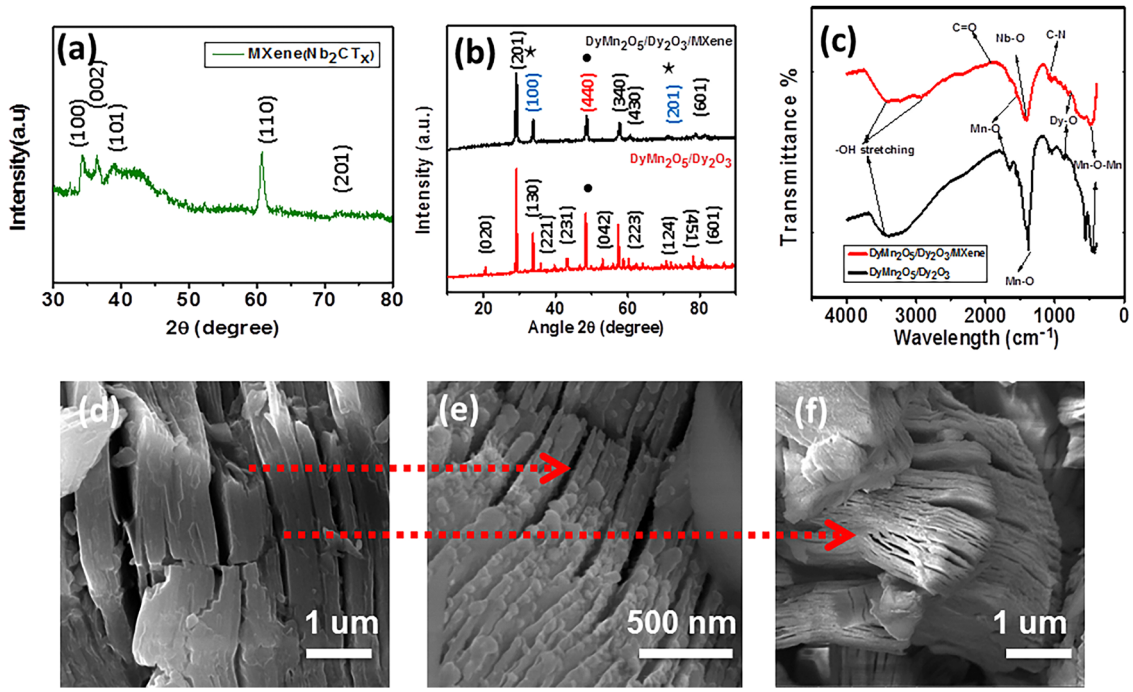


Fig. 3 (a) XRD pattern of $Nb_2CT_x$, (b) XRD spectrum of $DyMn_2O_5/Dy_2O_3$ and $DyMn_2O_5/Dy_2O_3$/MXene, (c) FTIR spectrum of both the $DyMn_2O_5/Dy_2O_3$ and $DyMn_2O_5/Dy_2O_3$/MXene composite at room temperature, (d) SEM pictograph of the MAX phase of $Nb_2AlCT_x$ at 1 μm magnification, and (e) and (f) SEM images of the layered structure of MXene at high magnification of 500 nm and 1 μm, respectively.

PDF card #15-0127. These peaks confirm the successful formation of $Nb_2CT_x$ MXene.

Fig. 3(d–f) illustrates the morphological characteristics of $Nb_2AlCT_x$ and $Nb_2CT_x$. As shown in Fig. 3(d), $Nb_2AlCT_x$ exhibits a well-ordered ternary layered structure with no visible delamination, and its surface remains clean and intact. In contrast, the SEM images of $Nb_2CT_x$ MXene in Fig. 3(e and f) captured at resolutions of 500 nm and 1 μm respectively, reveal a distinct stacked structure with well separated layers. This transformation indicates the effective removal of the Al atomic layer from $Nb_2AlCT_x$ through KOH etching, resulting in the characteristic layered morphology of $Nb_2CT_x$ MXene. These observations are consistent with the XRD results, further validating the successful synthesis of $Nb_2CT_x$ MXene.

Furthermore, Fig. 3(b) exhibits the XRD pattern of both synthesized samples. The characteristic peaks in the prepared sample $DyMn_2O_5/Dy_2O_3$ observed at $2\theta$ = 20.6°, 29.1°, 33.7°, 35.9°, 43.0°, 53.1°, 57.3°, 58.9°, 70.9°, 78.4°, and 80.7° correspond to the (020), (201), (130), (221), (231), (042), (340), (223), (124), (451), and (601) crystal planes of orthorhombic $DyMn_2O_5$ (JCPDS # 01-07-1696). The refined lattice parameters, $a$ = 7.290 Å, $b$ = 8.633 Å, and $c$ = 5.626 Å, exhibit strong agreement with standard values (7.2940, 8.5551, and 5.6875 Å, respectively). Additionally, a distinct peak at $2\theta$ = 48.44° (•) corresponds to the (440) plane of cubic $Dy_2O_3$ (JCPDS 00-022-0612), confirming the presence of $Dy_2O_3$ as a secondary phase. The XRD pattern of the synthesized $DyMn_2O_5/Dy_2O_3$/MXene composite, shown in Fig. 3(b), was recorded over a broad $2\theta$ range (10°–90°). The peaks at $2\theta$ = 29.1°, 57.8°, 60.7°, and 80.7° correspond to the (201), (340), (430), and (601) planes of orthorhombic $DyMn_2O_5$ (JCPDS 01-07-1696). Additionally, the peaks observed at $2\theta$ = 33.9° and 72.7° (★) correspond to the (100) and (201) planes of hexagonal niobium carbide ($Nb_2C$), indexed to JCPDS # 00-015-0127, confirming the incorporation of the MXene phase. The distinct peak at $2\theta$ = 48.44° (•) is also present in the composite sample, further verifying the coexistence of $Dy_2O_3$. The XRD pattern of the $DyMn_2O_5$ composite with MXene exhibits characteristic peaks corresponding to $DyMn_2O_5$, $Dy_2O_3$, and $Nb_2CT_x$, confirming the successful synthesis of the $DyMn_2O_5/Dy_2O_3$/MXene composite. The Debye–Scherrer formula was employed to assess the crystallite size:

$$D = \frac{K\lambda}{\beta \cos\theta} \quad (1)$$

where $D$ is crystallite size, $K$ = 0.9 (Scherrer constant), $\lambda$ = 0.15406 nm (wavelength of Kα X-ray sources), $\theta$ is peak position in radians and $\beta$ is full width and half maximum (FWHM). The obtained values of average crystallite size of $DyMn_2O_5/Dy_2O_3$ and $DyMn_2O_5/Dy_2O_3$/MXene composite size from eqn (1) are 61.9 nm and 39.4 nm, respectively, which confirms the nanoparticle (1–100 nm) behavior of both samples. In addition, the crystallite size has been calculated by the Williamson–Hall (W–H) model (eqn (2)) and modified Scherrer relation (eqn (3)) using eqn (2) and (3), respectively.

$$\beta_t \cos\theta = \varepsilon(4\sin\theta) + \frac{K\lambda}{D} \quad (2)$$

$$\ln(\beta) = \ln\left(\frac{1}{\cos\theta}\right) + \ln\left(\frac{K\lambda}{D}\right) \quad (3)$$

Both equations are the equations of a straight line, where $\frac{K\lambda}{D}$ and $\ln\left(\frac{K\lambda}{D}\right)$ respectively, are the $y$-intercepts of both equations from which crystallite size is measured by W–H plots and modified W–H plots as in Fig. S1(a–d) (ESI†). Also, it is very helpful to find strain by extracting the slope and $y$-intercept of the linear fit as demonstrated in Fig. S1(a and b) (ESI†). The estimated values of strain, crystallite size, dislocation density and crystallinity for both samples $DyMn_2O_5/Dy_2O_3$ and the $DyMn_2O_5/Dy_2O_3$/MXene composite are given in Table 1.

The crystallite size of $DyMn_2O_5/Dy_2O_3/Nb_2CT_x$ is smaller than that of $DyMn_2O_5/Dy_2O_3$, indicating a higher surface area, which can contribute to enhanced specific capacitance. Furthermore, the crystallite size estimated using the Williamson–Hall (W–H) plot method is observed to be smaller than that determined by Scherrer's equation. This discrepancy arises because the W–H model accounts for microstrain and instrumental broadening effects, making it a more accurate approach for crystallite size determination.[59] Dislocation density can provide details about the material's mechanical characteristics and deformation processes. The dislocation density of $DyMn_2O_5/Dy_2O_3$/MXene is more than that of $DyMn_2O_5/Dy_2O_3$, which informs us that the mechanical properties of the composite, especially its hardness and strength, have been improved.[60] Furthermore, the $DyMn_2O_5/Dy_2O_3$/MXene composite exhibits higher crystallinity compared to $DyMn_2O_5/Dy_2O_3$, indicating an increase in structural order. Crystallinity is a fundamental parameter that has a significantly impact in determining the overall electrochemical functionality of materials. Highly crystalline structures typically facilitate enhanced charge/discharge kinetics, improved electrical conductivity, and greater structural stability. Therefore, precise control over crystallinity through optimized synthesis and processing techniques is essential for tailoring the electrochemical properties of materials in energy storage and conversion applications.[61]

**3.1.2. FTIR analysis.** The FT-IR spectral analysis of the $DyMn_2O_5/Dy_2O_3$ and $DyMn_2O_5/Dy_2O_3$/MXene composite at room temperature is presented in Fig. 3(c) to elucidate its functional group characteristics and chemical bonding interactions in wavenumber range 0–4000 $cm^{-1}$. The FTIR spectrum of both synthesized nanocomposites displays a broad absorption band around 3456 $cm^{-1}$, attributed to the stretching vibrations of hydroxyl groups from adsorbed water molecules, while the peak at approximately 1674 $cm^{-1}$ corresponds to the bending vibrations of water molecules.[62] Similarly, in both composites, the peak positions at 447 $cm^{-1}$ can be assigned to the stretching vibrations of Mn–O–Mn bonds, while the peak at 803 $cm^{-1}$ can be ascribed to stretching vibration of Dy–O.[63,64] The presence of well-defined peaks at 1386 and 1668 $cm^{-1}$ corresponds to metal oxide (Mn–O) bonds in the crystal structure. The peak position at 1870 $cm^{-1}$ can be attributed to stretching vibrations of carbonyl groups C═O. A characteristic C–N stretching vibration has been detected at 1125 $cm^{-1}$ in the MXene structure.[65] Also, the vibration frequency at 1507 $cm^{-1}$ is characteristic of the Nb–O stretching mode.[66] The FT-IR spectrum of the composite material may offers critical insights into its electrochemical characteristics. The observed slight shift in peak position relative to the pristine $DyMn_2O_5/Dy_2O_3$ spectrum suggests modifications in the electronic structure arising from the incorporation of $Nb_2CT_x$. These structural alterations likely influence the material's electrochemical characteristics and efficiency by enhancing its redox activity by introducing additional redox-active sites.

**3.1.3. XPS analysis.** X-ray photoelectron spectroscopy (XPS) is conducted to elucidate the elemental makeup and oxidation states of the constituent elements in the $DyMn_2O_5/Dy_2O_3$/MXene composite. The acquired XPS survey spectrum, presented in Fig. 4(a), displays a wide-spectrum graph of DMO/DO/MX (in binding energy range 0–1200 eV) that distinctly confirms the presence of Dy, Mn, Nb, O, and C. Notably, no additional peaks corresponding to other elements were detected, Confirming he excellent compositional purity of the prepared material. Furthermore, the Gaussian fitting method was employed to accurately analyze the oxidation states of the constituent elements. The high resolution XPS spectrum of Dy 4d (Fig. 4(b)) exhibits sharp peaks at B.E of 154.5 and 155.6 eV, attributed to Dy $4d_{5/2}$ and Dy $4d_{3/2}$, respectively, proving the characteristic electronic states of dysprosium. One peak associated with 157.1 eV represents the existence of $Dy_2O_3$.[67,68]

The high-resolution XPS spectrum of Mn 2p (Fig. 4(c)) exhibits distinct peaks at 642.9 and 654.03 eV characteristic of Mn $2p_3/_2$ and Mn $2p_{1/2}$ spin–orbit components, respectively, while the peak at 647.6 eV represents a satellite peak. The measured spin–orbit splitting of 11.15 eV between these states is characteristic of $Mn^{3+}$ based materials, further confirming the oxidation state of manganese in the synthesized sample.[69] Fig. 4(d) presents the high-resolution XPS spectrum of Nb 3d, where the deconvolution of the $Nb^{4+}$ $3d_5/_2$ and $Nb^{4+}$ $3d_3/_2$ peaks reveals $Nb^{4+}$ oxidation states. The characteristic peak at 206.1 eV is attributed to Nb–C, while the characteristic peak at 208.9 eV corresponds to Nb–O bonding.[70,71] Fig. 4(e) presents

Table 1 A comparison in different parameters, measured from XRD data, for $DyMn_2O_5/Dy_2O_3$ and $DyMn_2O_5/Dy_2O_3$/MXene

| Sample | Crystallite size by Scherrer (nm) | Crystallite size by W–H model (nm) | Crystallite size by modified Scherrer's equation (nm) | Micro strain $\varepsilon \times 10^{-3}$ | Dislocation density $\delta \times 10^{-3}$ $(nm)^{-2}$ | Crystallinity (%) |
|---|---|---|---|---|---|---|
| $DyMn_2O_5/Dy_2O_3$ | 61.9 | 50.6 | 58.6 | 1.5 | 0.44 | 62.5 |
| $DyMn_2O_5/Dy_2O_3/Nb_2CT_x$ | 39.4 | 29.8 | 24.6 | 2.5 | 0.96 | 73.4 |

 

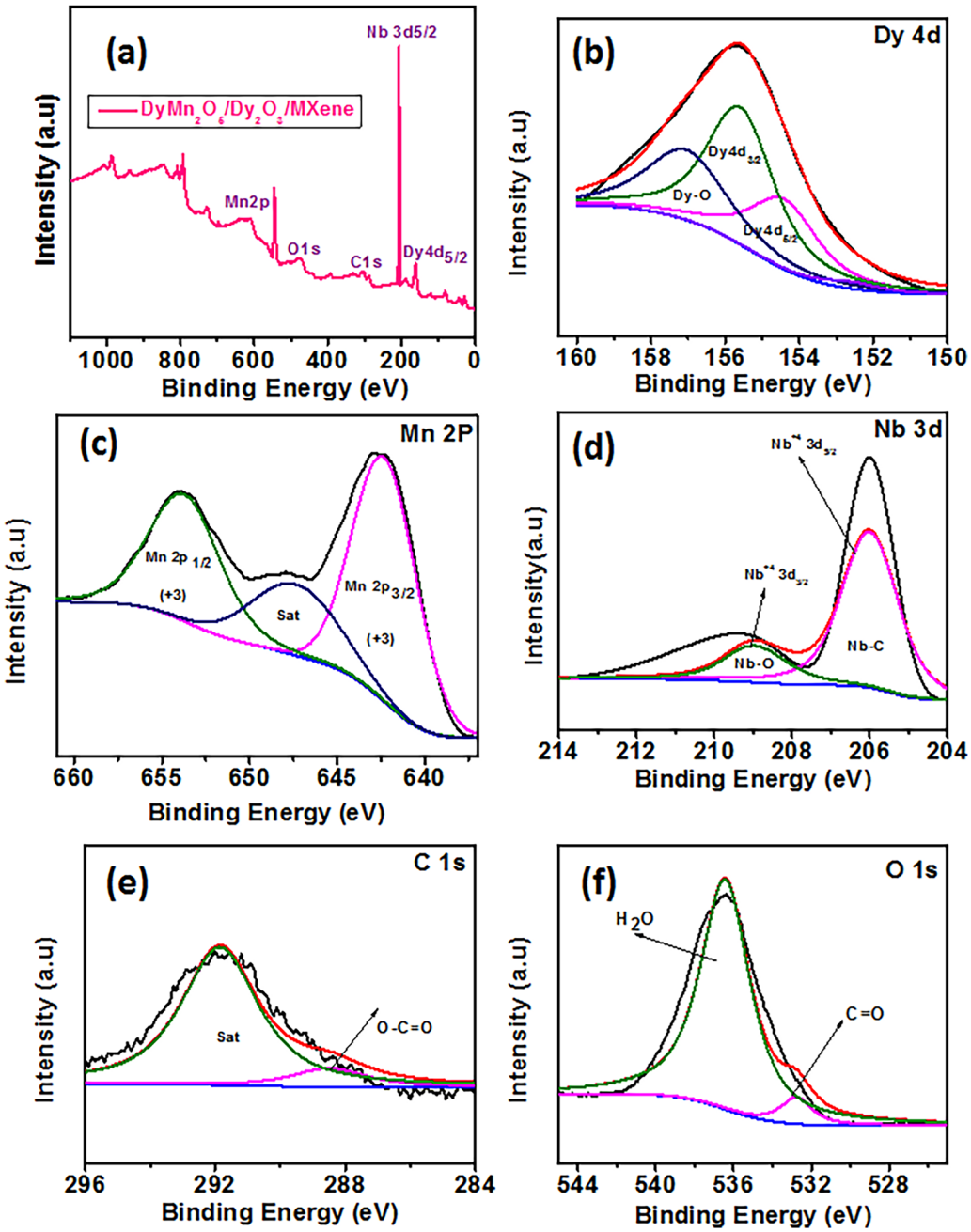


Fig. 4 (a) XPS wide spectrum graph of $DyMn_2O_5/Dy_2O_3$/MXene, and (b) high resolution spectra of Dy 4d, (c) of Mn 2P, (d) of Nb 3d, (e) of C 1s, and (f) of O 1s.

the high resolution XPS spectrum of C 1s, where the deconvolution reveals distinct spectral components. The peak observed at 288.2 eV corresponds to O–C═O, indicating modifications in the chemical state of carbon bonded to oxygen. Additionally, the peak at 291.2 eV is identified as a satellite peak, attributed to the presence of C–O functional groups, reflecting the electronic interactions within the material.[72] Fig. 4(f) depicts the high resolution XPS spectrum of O 1s, where one peak at 532.8 eV is due to chemisorbed oxygen and is also indicative of carbonyl (C═O) functional groups. Meanwhile, the peak at 536.4 eV is associated with adsorbed molecular oxygen ($O_2$) or surface-bound water ($H_2O$), suggesting the presence of physisorbed species on the material's surface.[73]

### 3.2. Morphological and compositional analysis

The surface morphology of the $DyMn_2O_5/Dy_2O_3$ and $DyMn_2O_5/Dy_2O_3$/MXene composites was systematically analyzed using scanning electron microscopy (SEM), and the corresponding micrographs, captured at varying magnifications, are depicted in Fig. 5 and 6. As observed in Fig. 5(a–c), the $DyMn_2O_5/Dy_2O_3$ sample exhibits a distinct assembly of peanut-shaped microparticles that are interconnected, forming a compact structure.

Fig. 5(d) demonstrates the energy-dispersive X-ray (EDX) spectrum of the as-synthesized $DyMn_2O_5$, where characteristic peaks confirm the presence of Dy (dysprosium), Mn (manganese), and O (oxygen), with their respective atomic and weight percentages detailed in the inset. The EDX analysis unequivocally verifies the compositional integrity of the synthesized material, further corroborated by X-ray diffraction (XRD) analysis. Moreover, statistical evaluation using ImageJ software, as depicted in the histogram of Fig. 5(e), indicates that the average length of the peanut-shaped $DyMn_2O_5/Dy_2O_3$ particles is approximately 0.34 μm.

Fig. 6(a and b) presents the SEM micrographs of the $DyMn_2O_5/Dy_2O_3$/MXene composite at magnifications of 500 nm and 2 μm. The images reveal the presence of small, variably sized cubic-shaped platelets, which are uniformly distributed across the two-dimensional $Nb_2CT_x$ (MXene) layer, with multiple interstitial voids between them. Fig. 6(d) displays the energy-dispersive X-ray (EDX) spectrum of the composite, confirming the presence of Dy (dysprosium), Mn (manganese), O (oxygen), Nb (niobium), and C (carbon), thereby substantiating the elemental composition of the as-synthesized material. Furthermore, statistical analysis performed using Image J software, as represented in the histogram of Fig. 6(e), indicates that the average particle size of the $DyMn_2O_5/Dy_2O_3$/MXene composite is approximately 78 nm. The extensive surface area of the MXene layers enhances heterogeneous nucleation, thereby promoting the formation of small nanoparticles. Additionally, the hydrophilic nature of MXene and the abundance of surface-anchored functional groups (*e.g.*, –OH, –F, –O) facilitates strong interactions with precursor ions, effectively regulating their diffusion dynamics and constraining particle growth, ultimately leading to a reduction in overall nanoparticle size. The surface morphology and small particle size of $DyMn_2O_5/Dy_2O_3$/MXene as compared to $DyMn_2O_5/Dy_2O_3$ gives active sites and facilitate diffusion of ions, which may ultimately improve electrochemical properties.

### 3.3. Electrochemical analysis

The electrochemical properties of the synthesized materials (DMO/DO and DMO/DO/MX) were systematically investigated using cyclic voltammetry (CV), galvanostatic charge discharge (GCD), and electrochemical impedance spectroscopy (EIS). Initially, the intrinsic electrochemical behavior of both samples was assessed through CV measurements employing a three-electrode system. In this setup, an Ag/AgCl electrode served as the reference, a platinum (Pt) wire functioned as the counter electrode, and the working electrode was composed of the synthesized material coated onto a nickel (Ni) foam substrate. Cyclic voltammetry (CV) measurements were conducted for all synthesized materials MXene ($Nb_2CT_x$), $DyMn_2O_5/Dy_2O_3$ and $DyMn_2O_5/Dy_2O_3$/MXene in a 3 M KOH electrolyte across a range of scan rates of 10, 20, 30, 40, 50 and 100 mV $s^{-1}$, within a potential window of 0.1–0.7 V. The corresponding CV profiles are presented in Fig. 7(a–c), illustrating the well-defined sharp redox peaks, which indicates pseudo capacitive behavior of all prepared samples. MXene CV curves, in this positive potential window (0.1–0.7 V), display pronounced redox peaks, indicating pseudocapacitive behavior. This is attributed to reversible faradaic reactions between the surface functional groups of the $Nb_2C$ MXene (*e.g.*, –OH, =O, –F) and the electrolyte ions. Nb-based MXenes, like other transition-metal carbides, can undergo surface redox reactions due to multiple oxidation states of Nb (*e.g.*, $Nb^{5+}/Nb^{4+}$), contributing to charge storage *via* pseudocapacitance. Meanwhile, DMO/DO and DMO/DO/MX also depict sharp redox peaks, confirming pseudocapacitive behavior. With increasing scan rates, redox peaks exhibit a shift towards higher potentials, indicating an enhancement in ion transport resistance, while the same shape of the CV curves

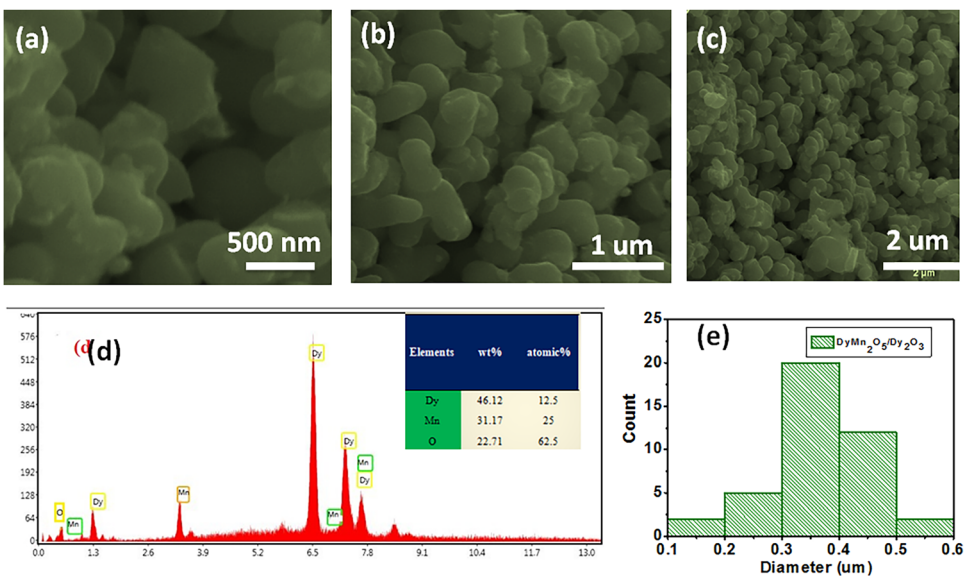


Fig. 5 (a)–(c) Scanning electron microscope (SEM) images of sample $DyMn_2O_5/Dy_2O_3$ at different magnifications (500 nm, 1–2 μm respectively). (d) EDX image of $DyMn_2O_5/Dy_2O_3$. (e) Histogram of the statistical distribution of lengths of particles of $DyMn_2O_5/Dy_2O_3$.

 

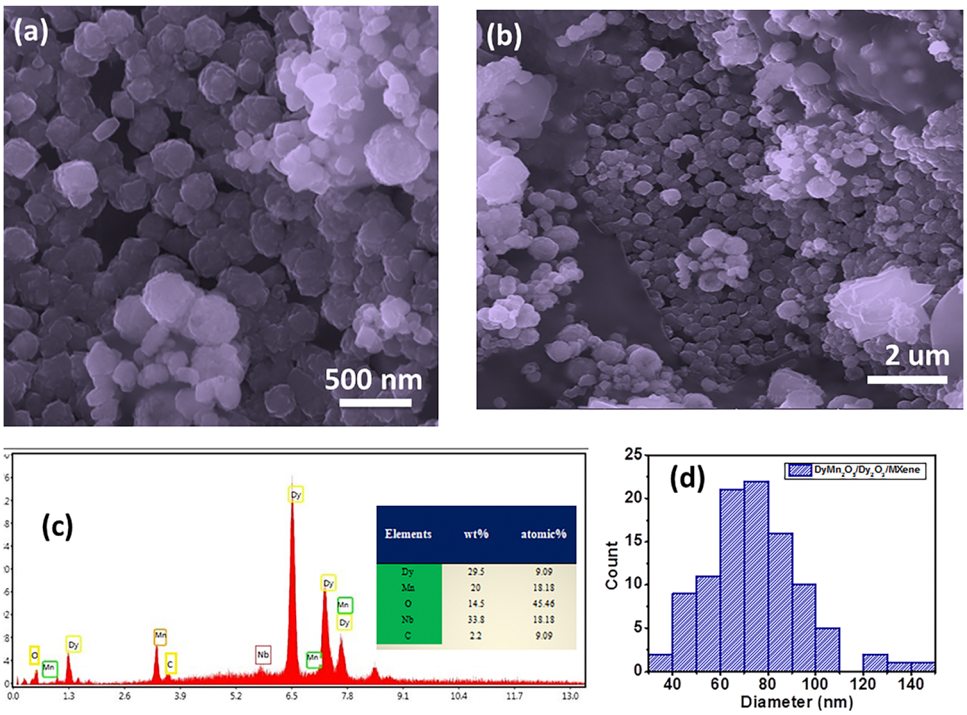


Fig. 6 (a) and (b) SEM pictographs of composite $DyMn_2O_5/Dy_2O_3$/MXene at different magnifications. (c) EDX image of $DyMn_2O_5/Dy_2O_3$ MXene. (d) Histogram of statistical distribution of lengths of particles in composite $DyMn_2O_5/Dy_2O_3$/MXene.

even at higher scan rates suggests efficient charge transfer dynamics and stable electrochemical behavior of the electrode material.[74,75] DMO/DO/MX demonstrates a large integrated area under the CV curve at 10 mV $s^{-1}$, indicating a significantly enhanced specific capacitance relative to DMO/DO as shown in Fig. 7(d). The specific capacitance of all electrodes, MXene, DMO/DO and DMO/DO/MX is determined through the following equations.[76]

$$C_s = \frac{\int I \times dv}{m \times k \times (\Delta V)} \quad (4)$$

where $\int I \times dv$ is the integral sweep area of the curve, $m$ is the active mass of the electrode, $(\Delta V)$ is potential window and $k$ denotes scan rate. The calculated specific capacitances of MXene are 105.9 F $g^{-1}$, 61.13 F $g^{-1}$, 50.24 F $g^{-1}$, 44.30 F $g^{-1}$, 39.10 F $g^{-1}$, and 23.92 F $g^{-1}$, for DMO/DO and 703.9 F $g^{-1}$, 394.5 F $g^{-1}$, 285.9 F $g^{-1}$, 241.2 F $g^{-1}$, 208.6 F $g^{-1}$ and 130.6 F $g^{-1}$, and for DMO/DO/MX are 863.1 F $g^{-1}$, 629.36 F $g^{-1}$, 530.2 F $g^{-1}$, 413.9 F $g^{-1}$, 368.3 F $g^{-1}$ and 213.9 F $g^{-1}$ at scan rates of 10 mV $s^{-1}$, 20 mV $s^{-1}$, 30 mV $s^{-1}$, 40 mV $s^{-1}$, 50 mV $s^{-1}$ and 100 mV $s^{-1}$, respectively (Table S1, ESI†). DMO/DO/MX has significantly high specific capacitance as compared to DMO/DO, which may be governed by the presence of $Nb_2CT_x$ MXene. $DyMn_2O_5$ undergoes redox reactions involving $Mn^{3+}/Mn^{2+}$ and $Mn^{4+}/Mn^{3+}$ transitions, while $Dy_2O_3$ dissolves in an alkaline medium, forming hydroxylated species and niobium carbide undergoes surface hydroxylation and redox reactions contributing to charge storage.

$$Mn_2O_5 + 2e^- + H_2O \leftrightarrow 2MnO_2 + 2OH^- \quad (5)$$

$$MnO_2 + e^- + OH^- \leftrightarrow MnOOH \quad (6)$$

$$Dy^{3+} + 3OH^- \leftrightarrow Dy(OH)_3 \quad (7)$$

$$Dy_2O_3 + 6OH^- + 3H_2O \leftrightarrow 2Dy(OH)_6^{-3} \quad (8)$$

$$Dy\,(OH)_3 + e^- \leftrightarrow Dy(OH)_2 + OH^- \quad (9)$$

$$Nb_2C + 2OH^- \leftrightarrow Nb_2C\,(OH)_2 + 2e^- \quad (10)$$

$$Nb_2C + 4OH^- \leftrightarrow 2NbO\,(OH) + 2H_2O + 4e^- \quad (11)$$

$$NbO\,(OH) + e^- + OH^- \leftrightarrow NbO_2 + H_2O \quad (12)$$

The electrochemical performance of the DMO/DO/MX system is predominantly governed by faradaic redox transitions involving Mn, Dy, and Nb species, which contribute to charge storage. Additionally, the surface hydroxylation of $Nb_2C$ enhances its pseudocapacitive behavior, while the 3 M KOH alkaline electrolyte supplies hydroxyl ions, facilitating ion transport and interfacial redox reactions. Various methodologies have been proposed for distinguishing between diffusion-controlled and capacitive (non-diffusion-limited) processes. Dunn (2007) introduced a normalization formula for cyclic voltammetry (CV) kinetics analysis, as represented in eqn (13). Using this approach, the contributions of capacitive and diffusion-controlled processes in the DMO/DO/MX electrode were quantified based on the given equation.[77]

$$i(v) = k_1(V) + k_2(V)^{1/2} = i\,(\text{capacitive}) + i\,(\text{diffusion}) \quad (13)$$

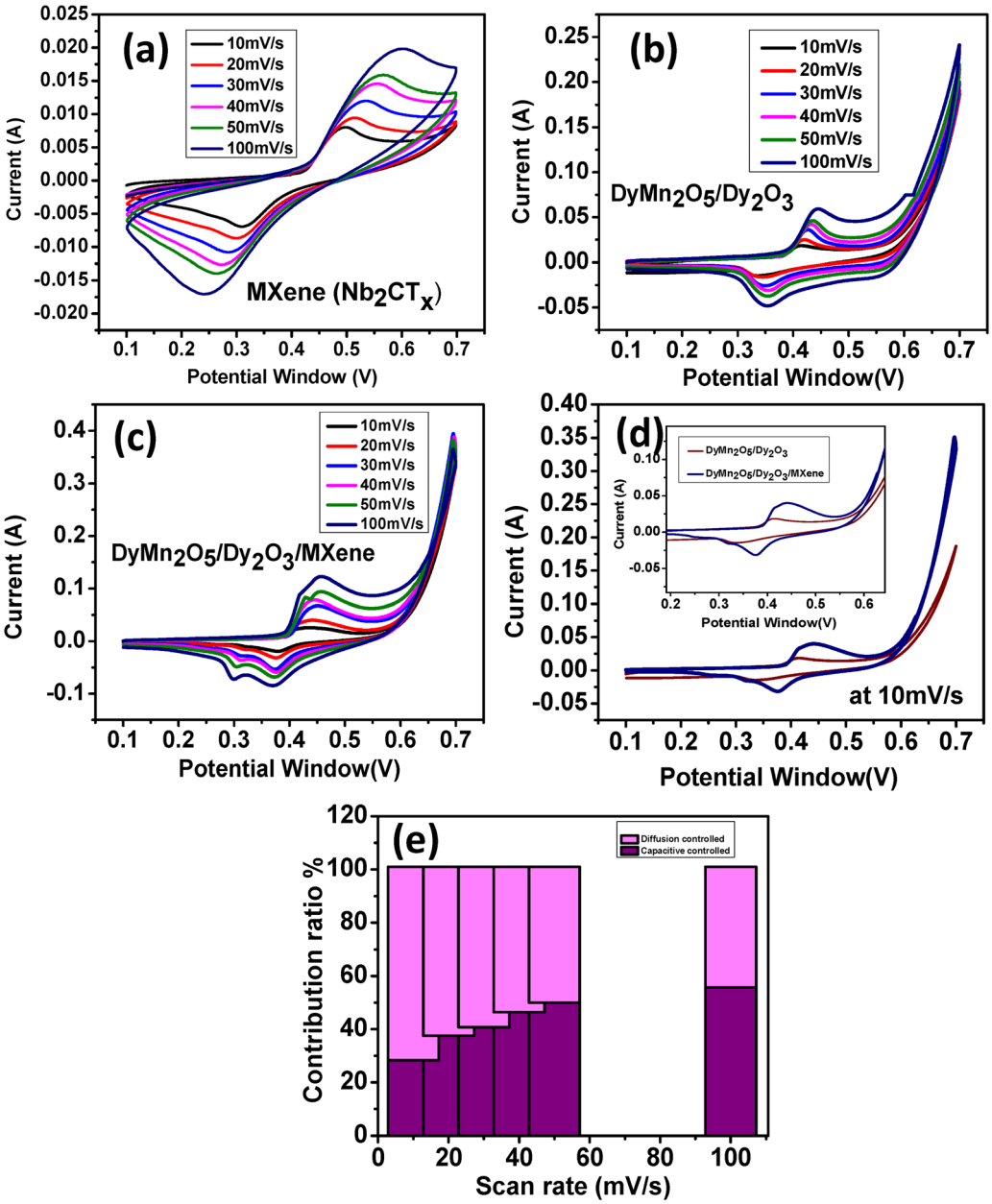


Fig. 7 (a) CV curves of MXenes at different scan rates, (b) and (c) CV curves of DMO/DO and DMO/DO/MX at different scan rates (10–100 mV $s^{-1}$), (d) comparison of the CV curves of DMO/DO and DMO/DO/MX at 10 mV $s^{-1}$ and (e) capacitive and diffusion-controlled contributions in DMO/DO/MX at different scan rates.

In this context, $i(v)$ represents the current at a given potential $V$, while $k_1(V)$ and $k_2(V)^{1/2}$ correspond to the contributions from diffusion limiting (surface capacitive effects) and diffusion-controlled processes, respectively. The graphical representation highlights the dual influence of capacitive effects and ion diffusion on the total capacitance. Furthermore, Fig. 7(e) depicts the total capacitance contribution of the DMO/DO/MX electrode at a scan rate of 20 mV $s^{-1}$. At scan rates of 10, 20, 30, 40, 50, and 100 mV $s^{-1}$, the electrode DMO/DO/MX exhibits diffusion controlled contributions of 72.61%, 63.41%, 60.28%, 54.59%, 51.01%, and 45.26%, respectively. Notably, the diffusion controlled contribution of the DMO/DO/MX electrode dominates, which confirms the pseudo capacitive behavior. At higher scan rates, the time available for ion diffusion decreases, thus enhancing the capacitive controlled contribution.

Fig. 8(a) shows the galvanostatic charge discharge (GCD) curves of $Nb_2CT_x$ MXene at 1, 2, 3 and 5 A $g^{-1}$. Fig. 8(b) presents the comparison of the GCD curves of DMO/DO and DMO/DO/MX electrodes recorded across a current density of 1 A $g^{-1}$ within the potential window (0–0.5 V), providing insights into their electrochemical performance under charge discharge conditions. The observed reduction in the potential window during GCD measurements as compared to CV curves can be attributed to internal resistance, kinetic constraints of redox

 

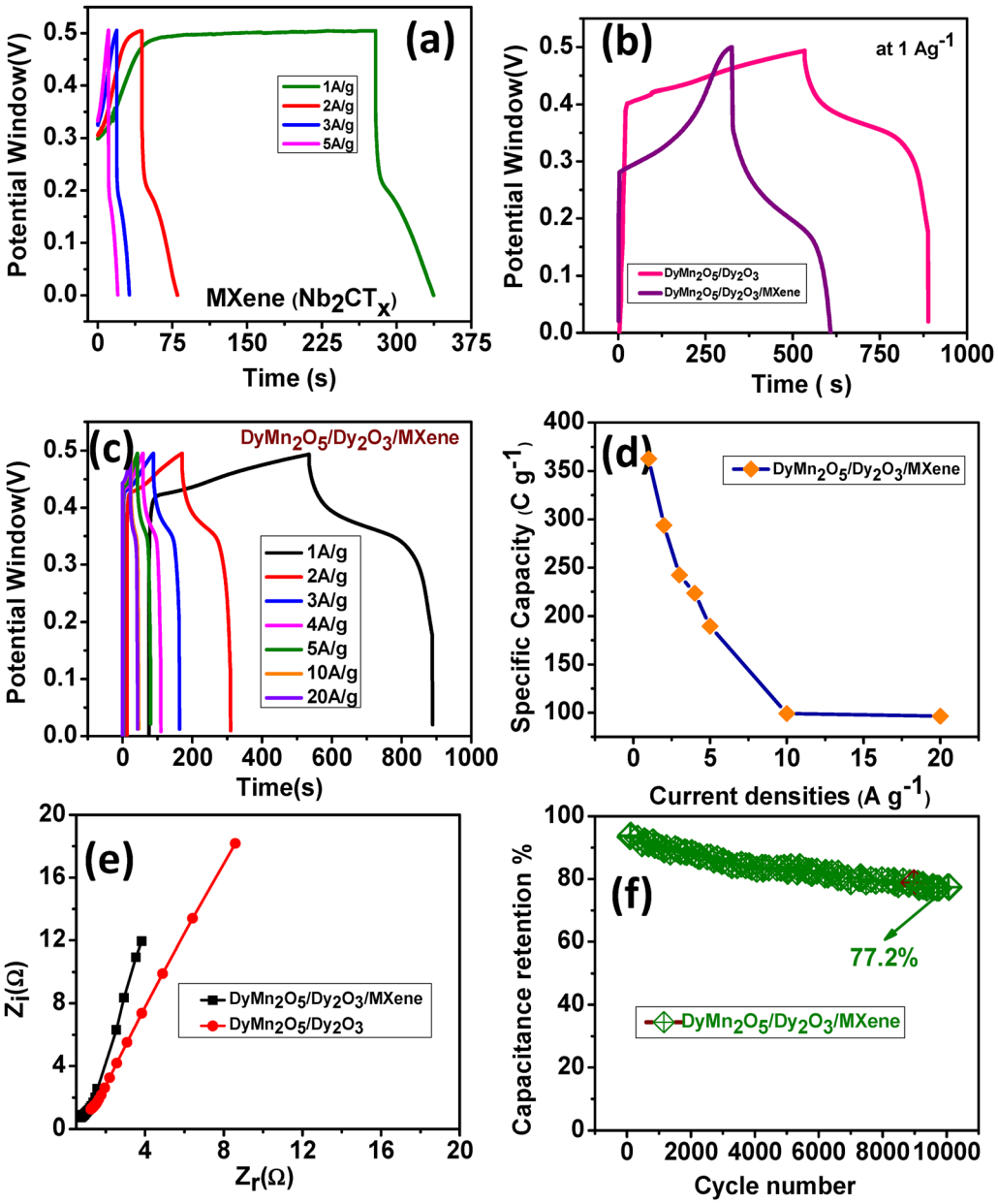


Fig. 8 (a) GCD curves of MXene ($Nb_2CT_x$) at different current densities, (b) comparison of the GCD curves of DMO/DO and DMO/DO/MX at 1 A $g^{-1}$, (c) GCD curves of DMO/DO/MX at different current densities (1–20 A $g^{-1}$), (d) trend depicting that $C_s$ decreases as current density increases, (e) Nyquist plot of DMO/DO and DMO/DO/MX, and (f) cycling stability of DMO/DO/MX at 5 A $g^{-1}$ over 10 000 cycles.

reactions, and the need to avoid electrolyte decomposition at higher potentials. All electrodes demonstrate a nonlinear charge–discharge curve, confirming the characteristic of purely faradaic behavior of both materials, and also supported the CV results by suggesting a diffusion-controlled redox process. Notably, the DMO/DO/MX electrode exhibits the longest discharge duration as compared to DMO/DO, indicating its superior specific capacity. MXene, DMO/DO and DMO/DO/MX exhibit specific capacity of 70.23 C $g^{-1}$, 285.41 C $g^{-1}$ and 362.92 C $g^{-1}$ respectively at 1 A $g^{-1}$ within a potential window of 0–0.5 V.

Fig. 8(c) exhibits GCD curves of DMO/DO/MX at different current densities 1, 2, 3, 4, 5, 10 and 20 A $g^{-1}$ within a potential window of 0–0.5 V. The specific capacity ($C_s$) from GCD curves of DMO/DO/MX at different current densities is calculated using the following formula[78,79]

$$C_s = \frac{I \times t}{m} \quad (14)$$

where $C_s$ denotes the specific capacity (C $g^{-1}$), $I$ is the discharge current in amperes (A), $t$ is the discharge time (s), and $m$ represents the mass of the active electrode material (g). The specific capacity obtained from eqn (14) is 362.92, 293.78, 242.43, 223.44, 189.55, 99.21, and 96.4 C $g^{-1}$ at 1, 2, 3, 4, 5, 10 and 20 A $g^{-1}$, respectively. The nonlinear nature of the GCD curves, along with the evident potential drops at elevated

current densities, suggest a limited availability of active sites within the nanocomposites DMO/DO/MX ultimately leading to a reduction in specific capacity from 362.92 to 96.4 C $g^{-1}$ (Table S2, ESI†). DMO/DO/MX exhibits prolonged discharge duration and high specific capacity, which can be attributed to a synergistic effect arising from $DyMn_2O_5$, $Dy_2O_3$ and $Nb_2C$, improved electrical conductivity due to MXene layers, efficient and deep electrolyte penetration, large surface area due to MXene layers and also the multiple oxidation states of all metals as confirmed by XPS. With increasing current density, the specific capacity of the DMO/DO/MX electrode gradually declines (Fig. 8(d)). This reduction can be attributed to the limited faradaic response and the intrinsic resistance of the synthesized material under high current conditions.[80] Table 2 presents a comparative analysis of the specific capacitance of the DMO/DO/MX sample synthesized *via* a simple hydrothermal method in relation to recently reported materials.

Electrochemical impedance spectroscopy was used to study the impedance behavior of both electrode materials in the frequency range of 0.1 to $10^5$ Hz with a small amplitude of 5 mV to ensure system linearity and maintain data quality during measurement. Fig. 8(e) exhibits Nyquist plots of both electrodes. In general, a Nyquist plot consists of two parts, the first part consists of a semicircle in the high frequency range and the other part represents an inclined line in the low frequency range.[81] The resistance of the electrode material, electrolyte and interface of the electrolyte and electrode material can be determined by the *x*-intercept at a high frequency range, termed as solution resistance "$R_s$". The charge transfer resistance "$R_{ct}$" at the electrode material is determined by the diameter of the semicircle.[73] The DMO/DO/MX electrode exhibits a relatively low charge transfer resistance ($R_{ct}$ = 10.1 Ω) as compared to DMO/DO (13.9 Ω) indicating the enhanced capacitive performance of the DMO/DO/MX electrode. Furthermore, the Nyquist plot for DMO/DO/MX exhibits a steeper slope in the low-frequency region, with a greater inclination toward the imaginary axis.

This characteristic suggests a lower diffusion resistance compared to the other electrodes, indicating improved ion transport dynamics.[82] These results indicate that the DMO/DO/MX electrode possesses inherently lower resistance, facilitating more efficient ion transport and electron transfer. This enhanced conductivity contributes to its high specific capacitance and stable cycling performance. The cycling lifespan of a supercapacitor is a critical parameter that significantly influences its practical applicability and long-term performance. Fig. 8(f) exhibits that the DMO/DO/MX electrode maintained 77.2% of its initial capacitance after 10 000 charge–discharge cycles at a current density of 5 $Ag^{-1}$. These findings demonstrate that the $DyMn_2O_5/Dy_2O_3$ composite with MXene significantly gives a high specific capacitance with long-life stability, making it a promising candidate for pseudo capacitor applications.

The enhanced specific capacitance and cycling stability of the $DyMn_2O_5/Dy_2O_3$ decorated MXene composite can be attributed to several inter-related mechanisms. Firstly, the presence of dysprosium (Dy) ions plays a crucial role in improving capacitive behavior through reversible redox reactions involving $Dy^{3+}/Dy^{2+}$ and $Mn^{4+}/Mn^{3+}$ couples. These redox transitions contribute additional faradaic charge storage, boosting the overall capacitance. Secondly, $DyMn_2O_5$ and $Dy_2O_3$ nanoparticles provide multiple active sites for electrochemical reactions, while their stable crystal structures enhance cycling durability. When integrated with MXene, a highly conductive and layered 2D material, a strong interfacial synergy emerges. MXene acts as a conductive backbone that accelerates electron transport and minimizes internal resistance, while also serving as a mechanically robust support that accommodates volume changes during charge–discharge cycles. This synergistic interaction between the redox active rare earth oxides and the conductive MXene matrix leads to improved charge storage kinetics, higher specific capacity, and excellent long term cycling stability.[58,83,84]

### 3.4. Assembly of an asymmetric super capacitor (ASC) using $DyMn_2O_5/Dy_2O_3$/MXene‖AC

The remarkable electrochemical performance of the $DyMn_2O_5/Dy_2O_3$/MXene composite necessitated a comprehensive evaluation of its energy storage potential for practical applications. To assess its practical viability, an asymmetric supercapacitor (ASC) was fabricated, integrating DMO/DO/MX as the positive electrode and activated carbon (AC) as the negative electrode (designated as DMO/DO/MX‖AC ASC). The 2 M KOH electrolyte was utilized to enhance ionic conductivity and facilitate efficient charge transfer between the electrodes. The active loaded mass of DMO/DO/MX was approximately 3.2 mg. Fig. 9(a) presents the cyclic voltammetry (CV) curves of the DMO/DO/MX and Activated carbon (AC) at different potential windows and at the same scan rate of 10 mV $s^{-1}$. CV experiments were performed over progressively wider potential windows ranging

Table 2 Comparison of the electrochemical performance of the synthesized DMO/DO/MX in this work and recent reported work

| S. no. | Material | Specific capacitance (F $g^{-1}$) | Morphology | Synthesis method | Ref. |
|---|---|---|---|---|---|
| 1 | $SrMnO_3$ | 446 F $g^{-1}$ at 1 A $g^{-1}$ | Nano fibers | Sol gel | 85 |
| 2 | $CeO_2/LaMnO_3$ | 262 F $g^{-1}$ at 1 A $g^{-1}$ | Spherical nanoparticles | Co-precipitation | 86 |
| 3 | $DyMnO_3$ | 531 F $g^{-1}$ at 1 A $g^{-1}$ | | Microwave-assisted synthesis | 87 |
| 4 | $Dy_2NiMnO_6$ | 395.2 F $g^{-1}$ at 0.5 A $g^{-1}$ | Mesoporous sphere | Hydrothermal | 88 |
| 5 | $La_2CuMnO_6$ | 206 F $g^{-1}$ at 1 A $g^{-1}$ | Nanostructures | Hydrothermal | 89 |
| 6 | $Y_2NiMnO_6$ | 78 F $g^{-1}$ at 1 A $g^{-1}$ | Nanowires | Hydrothermal | 90 |
| 7 | α-$MnO_2$ | 111 F $g^{-1}$ at 5 mV $s^{-1}$ | Nanorods | Hydrothermal | 91 |
| 8 | $DyMn_2O_5/Dy_2O_3$/MXene | 725.8 F $g^{-1}$ at 1 A $g^{-1}$ | Cubic pallets | Hydrothermal | This work |

 

from 1.1 to 1.5 V at 20 mV $s^{-1}$ as depicted in Fig. 9(b). As the potential window increased, the enclosed area of each CV curve expanded, reflecting the greater energy stored at the enlarged operating potential window of 1.5 V. Above 1.5 V, oxygen evolution occurs, limiting the stability of the device. Consequently, 1.5 V was adopted as the maximum operating potential window for all subsequent electrochemical measurements of the ASC device. As anticipated, the fabricated asymmetric device achieves an extended operating voltage of 1.5 V, attributed to the synergistic integration of the electrochemically stable DMO/DO/MX positive electrode and the robust AC negative electrode.[92] CV curves of DMO/DO/MX//AC were recorded at scan rates ranging from 3 to 80 mV $s^{-1}$ within an operational voltage window of 0–1.5 V, as illustrated in Fig. 9(c). The presence of distinct redox peaks at 1.27 V and 0.80 V signifies a predominantly faradaic charge storage mechanism indicating pseudocapacitive behavior. A progressive increase in peak current was recorded with no significant distortion in the shape of the CV curves, even at higher scan rates, indicating the fabricated ASC's excellent rate capability and superior electrochemical reversibility. The GCD curves presented in Fig. 9(d) exhibit a non-linear quasi triangle shaped curve, reflecting efficient charge storage dynamics and favorable pseudocapacitive characteristics. The specific capacitance of the fabricated device, determined from the GCD curves was measured as 148.2, 84.5, 76.38, 72.4, 70.02, 68.1 and 60.2 F $g^{-1}$ at current

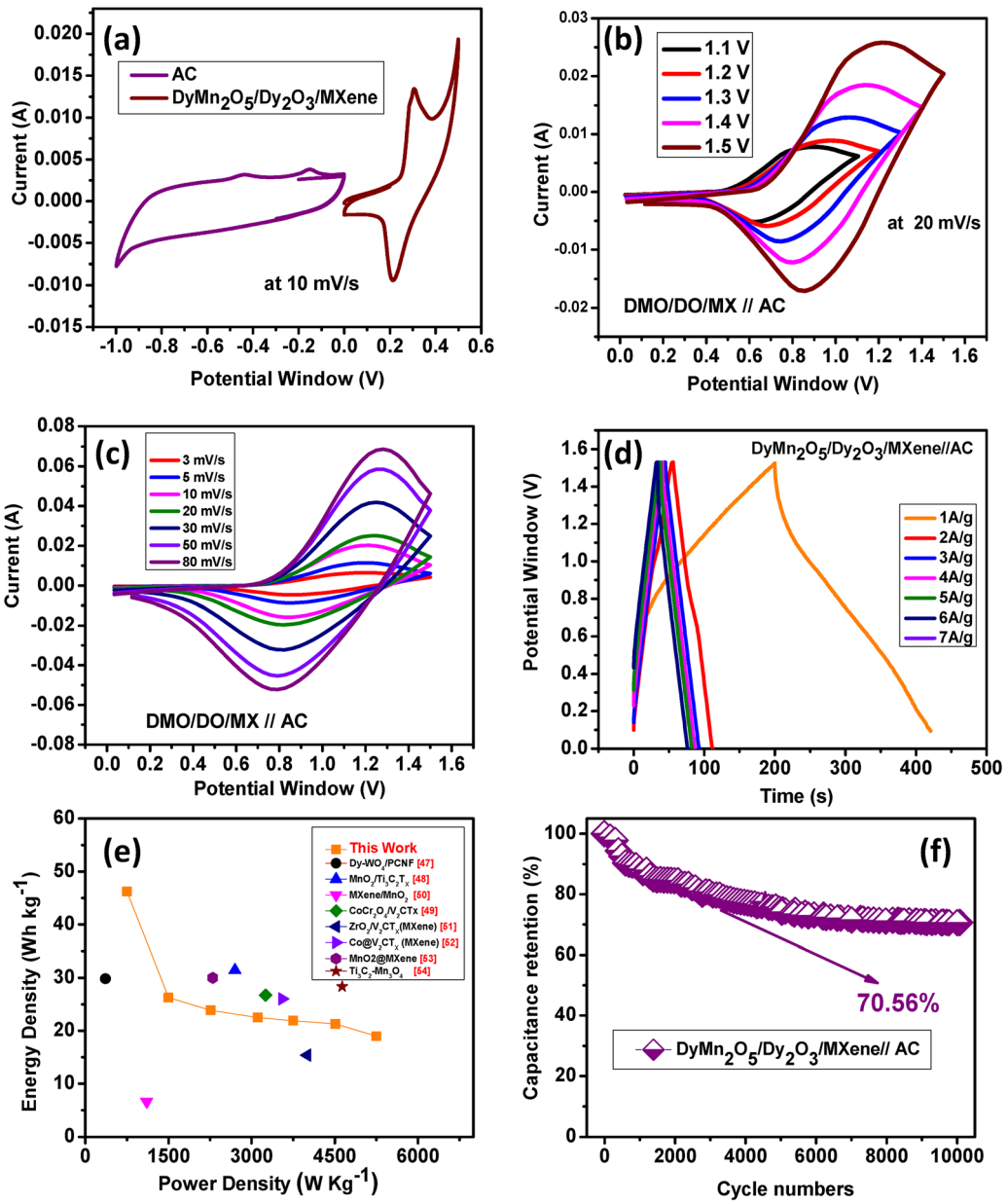


Fig. 9 (a) CV curves of AC and DMO/DO/MX at different potential windows at 10 mV $s^{-1}$, (b) CV curves of DMO/DO/MX//AC at different potential windows from 1.1–1.5 V at 20 mV $s^{-1}$ and (c) CV curves of DMO/DO/MX//AC at different scan rates from 3–80 mV $s^{-1}$. (d) GCD curves of DMO/DO/MX//AC at 1, 2, 3,4, 5, 6 & 7 A $g^{-1}$. (e) Ragone plot of DMO/DO/MX//AC. (f) Cyclic stability of DMO/DO/MX//AC during 10 000 cycles.

densities of 1, 2, 3, 4, 5, 6 and 7 A $g^{-1}$, respectively. The energy density ($E_d$) and the critical performance metric, power density ($P_d$), serve as fundamental parameters for assessing the energy efficiency of the fabricated asymmetric device and they are calculated from the GCD curves using the following equations.[93]

$$E_d = (C_s \times \Delta V^2)/(2 \times 3.6) \quad (15)$$

$$P_d = \frac{E}{\Delta t} \quad (16)$$

Fig. 9(e) illustrates the Ragone plot of the $DyMn_2O_5/Dy_2O_3$/MXene//AC ASC, demonstrating that the fabricated device achieves a high energy density of 46.25 W h $kg^{-1}$ at a power density of 750 W $kg^{-1}$. Furthermore, it retains an energy density of 18.96 W h $kg^{-1}$ even at a maximum power density of 5250.20 W $kg^{-1}$. This performance is comparable to, and in certain aspects surpasses, previously reported transition and rare earth-based metal oxides and MXene-based supercapacitors such as $MnO_2$@CNT//AC (13.4 W h $kg^{-1}$ at 602 W $kg^{-1}$),[94] $Ti_3C_2T_x$–δ-$MnO_2$//AC (8.2 W h $kg^{-1}$ at 400 W $kg^{-1}$),[95] λ-$MnO_2$//$Ti_3C_2T_x$ (15.5 W h $kg^{-1}$ at 100 W $kg^{-1}$),[96] Ni dope $CeO_2$@ d-$Ti_3CN$ (4.4 W h $kg^{-1}$ at 495 W $kg^{-1}$),[97] Dy doped $CoFe_2O_4$ (15.23 W h $kg^{-1}$ at 450 W $kg^{-1}$)[98] and $CeO_2/LaMnO_3$//AC (17.2 W h $kg^{-1}$ at 1015 W $kg^{-1}$).[86] The cycling stability of the DMO/DO/MX‖AC ASC was evaluated at a current density of 2 A $g^{-1}$ over 10 000 charge–discharge cycles (Fig. 9(f)), demonstrating a capacitance retention of 70.56%. This high retention exhibits the device's excellent stability and highlights its potential for high performance asymmetric supercapacitor (ASC) applications.

In this study, the fabricated system introduces a straightforward approach for synthesizing $Nb_2CT_x$-based MXene and rare earth metal-based oxide composites with outstanding cycling stability and high specific capacitance. This research offers innovative approaches for the development of flexible electrode materials with superior electrochemical performance, paving the way for next-generation portable and wearable electronic devices.

## Conclusions

In this study, a novel rare earth-based bi-metallic oxide $DyMn_2O_5/Dy_2O_3$/MXene nanocomposite was successfully synthesized using a hydrothermal method to enhance the interlayer spacing of MXene for improved electrochemical performance. The incorporation of $DyMn_2O_5/Dy_2O_3$ nanoparticles effectively mitigated the restacking issue of MXene, leading to an optimized electrode material with a high specific capacitance of 362.92 C $g^{-1}$ at 1 A $g^{-1}$ with 77% capacitance retention over 10 000 discharge cycles. Furthermore, an asymmetric supercapacitor assembled with the $DyMn_2O_5/Dy_2O_3$/MXene electrode and an activated carbon cathode exhibited a commendable energy density of 46.825 W h $kg^{-1}$ at a power density of 750 W $kg^{-1}$, retaining 70.56% of its initial capacitance after 10 000 cycles at 2 A $g^{-1}$. These findings highlight the potential of rare earth-based MXene nanocomposites as high-performance electrode materials for next-generation supercapacitors, demonstrating the effectiveness of the hydrothermal approach in tailoring nanostructured materials for energy storage applications.

## Author contributions

Komal Ali Rao: the conceptualization, formal analysis, investigation, methodology, data curation, software, writing original draft, editing and review, Javed Ahmad, Muhammad Bilal: resources and review Muhammad Ehsan Mazhar, Muhammad Imran Khan, Muhammad Suleman Ahmad, Muhammad Aziz and Hafeez ur rehman: review.

## Data availability

All data generated or analyzed during this study are included in this article. Furthermore all the related data are available from the authors upon request.

## Conflicts of interest

The authors declare that they have no known competing financial interest or personal relationships that could have appeared to influence the work reported in this paper.

## Acknowledgements

This research article is part of the PhD research work of Komal Ali Rao performed at the Institute of Physics, Bahauddin Zakariya University Multan, Pakistan.

## References

1 L. Bird, M. Milligan and D. Lew, *Integrating variable renewable energy: Challenges and solutions*, National Renewable Energy Lab.(NREL), Golden, CO, United States, 2013.
2 F. Ahmad, *et al.*, A highly active, low-cost CoZn ferrite electrocatalyst in oxygen reduction reactions, *Results Chem.*, 2025, 102095.
3 X. Chen, *et al.*, Lithium insertion/extraction mechanism in $Mg_2Sn$ anode for lithium-ion batteries, *Intermetallics*, 2024, **169**, 108306.
4 Y. Zhan, *et al.*, Enhancing prediction of electron affinity and ionization energy in liquid organic electrolytes for lithium-ion batteries using machine learning, *J. Power Sources*, 2025, **629**, 235992.
5 J. Liu, *et al.*, Advanced energy storage devices: basic principles, analytical methods, and rational materials design, *Adv. Sci.*, 2018, **5**(1), 1700322.
6 W. Abbas, *et al.*, Study of the electrical properties and electrochemical sensing efficiency of hydrothermally synthesized Sr doped Nickel oxide nanomaterials, *Phys. Scr.*, 2022, **97**(7), 075004.

 

7 M. Khalil, *et al.*, A critical review of biofuel cell cathodes, *Biofuels, Bioprod. Biorefin.*, 2025, DOI: 10.1002/bbb.2754.
8 F. Ahmad, *et al.*, Direct electron transfer chemistry of redox-active enzymes: applications in biosensor development, *Biofuels, Bioprod. Biorefin.*, 2025, DOI: 10.1002/bbb.2742.
9 X. Guo, *et al.*, Non-coordinating charge transfer enables ultrafast desolvation of hydrated zinc ions in the outer Helmholtz layer for stable aqueous Zn metal batteries, *Natl. Sci. Rev.*, 2025, **12**(4), nwaf070.
10 J. R. Miller and P. Simon, Electrochemical capacitors for energy management, *Science*, 2008, **321**(5889), 651–652.
11 X. Jian, *et al.*, Carbon-based electrode materials for supercapacitor: progress, challenges and prospective solutions, *J. Electr. Eng*, 2016, **4**(2), 75–87.
12 Z. Wang, *et al.*, Enhancing battery performance under motor overload drive with a battery–supercapacitor hybrid energy storage system, *J. Power Sources*, 2025, **642**, 236680.
13 L. Gao, *et al.*, Nitrogen-doped carbon trapped MnMoO4 microrods toward high performance aqueous zinc-ion battery, *J. Alloys Compd.*, 2023, **968**, 172008.
14 D. Cai, *et al.*, Binder-Free MOF-Based and MOF-Derived Nanoarrays for Flexible Electrochemical Energy Storage: Progress and Perspectives, *Small*, 2024, **20**(12), 2305778.
15 L. Gao, *et al.*, Zinc selenide/cobalt selenide in nitrogen-doped carbon frameworks as anode materials for high-performance sodium-ion hybrid capacitors. Advanced Composites and Hybrid, *Materials*, 2024, **7**(5), 144.
16 B. E. Conway, *Electrochemical supercapacitors: scientific fundamentals and technological applications*, Springer Science & Business Media, 2013.
17 P. Sinha and K. K. Kar, *Introduction to supercapacitors, in Handbook of Nanocomposite Supercapacitor Materials II: Performance*, Springer, 2020, pp. 1–28.
18 P. Biesheuvel, Y. Fu and M. Z. Bazant, Diffuse charge and faradaic reactions in porous electrodes, *Phys. Rev. E: Stat., Nonlinear, Soft Matter Phys.*, 2011, **83**(6), 061507.
19 X. Zhu, Recent advances of transition metal oxides and chalcogenides in pseudo-capacitors and hybrid capacitors: A review of structures, synthetic strategies, and mechanism studies, *J. Energy Storage*, 2022, **49**, 104148.
20 P. Bhojane, Recent advances and fundamentals of Pseudo-capacitors: Materials, mechanism, and its understanding, *J. Energy Storage*, 2022, **45**, 103654.
21 K. K. Patel, *et al.*, Evolution and recent developments of high performance electrode material for supercapacitors: A review, *J. Energy Storage*, 2021, **44**, 103366.
22 Z. Zhu, H. Peelaers and C. G. Van de Walle, Electronic and protonic conduction in $LaFeO_3$, *J. Mater. Chem. A*, 2017, **5**, 15367–15379.
23 Q. Hu, *et al.*, Facile syntheses of cerium-based $CeMO_3$ (M= Co, Ni, Cu) perovskite nanomaterials for high-performance supercapacitor electrodes, *J. Mater. Sci.*, 2020, **55**, 8421–8434.
24 B. Akinwolemiwa, C. Peng and G. Z. Chen, Redox electrolytes in supercapacitors, *J. Electrochem. Soc.*, 2015, **162**(5), A5054.
25 M. Majumder, *et al.*, Rare earth metal oxide (RE 2 O 3; RE= Nd, Gd, and Yb) incorporated polyindole composites: gravimetric and volumetric capacitive performance for supercapacitor applications, *New J. Chem.*, 2018, **42**(7), 5295–5308.
26 J. Lu, *et al.*, Effectively suppressing dissolution of manganese from spinel lithium manganate via a nanoscale surface-doping approach, *Nat. Commun.*, 2014, **5**(1), 5693.
27 S. Yang, *et al.*, Studies of structure and cycleability of $LiMn_2O_4$ and $LiNd_{0.01}Mn_{1.99}O_4$ as cathode for Li-ion batteries, *Electrochim. Acta*, 2003, **48**(5), 569–573.
28 R. Singhal, *et al.*, Synthesis and characterization of Nd doped LiMn2O4 cathode for Li-ion rechargeable batteries, *J. Power Sources*, 2007, **164**(2), 857–861.
29 P. Ram, *et al.*, Improved performance of rare earth doped $LiMn_2O_4$ cathodes for lithium-ion battery applications, *New J. Chem.*, 2016, **40**(7), 6244–6252.
30 Y. Xie, *et al.*, Synthesis and electrochemical properties of Sc-doped $Li_{1.05}Sc_xMn_{2-x}O_4$ spinel as cathodic material for rechargeable Li-battery, *Solid State Ionics*, 2005, **176**(35–36), 2563–2569.
31 H. Zhao, *et al.*, Rare earth incorporated electrode materials for advanced energy storage, *Coord. Chem. Rev.*, 2019, **390**, 32–49.
32 S. Liang, *et al.*, Rare-earth based nanomaterials and their composites as electrode materials for high performance supercapacitors: a review, *Sustainable Energy Fuels*, 2020, **4**(8), 3825–3847.
33 H. Huang and J.-J. Zhu, The electrochemical applications of rare earth-based nanomaterials, *Analyst*, 2019, **144**(23), 6789–6811.
34 J. T. Mefford, *et al.*, Anion charge storage through oxygen intercalation in LaMnO3 perovskite pseudocapacitor electrodes, *Nat. Mater.*, 2014, **13**(7), 726–732.
35 S. Demirel, *et al.*, Structural, magnetic, electrical and electrochemical properties of $SrCoO_{2.5}$, $Sr_9Co_2Mn_5O_{21}$ and $SrMnO_3$ compounds, *Ceram. Int.*, 2017, **43**(17), 14818–14826.
36 T. Sharmili, *et al.*, Investigation on $Y_2NiMnO_6$ nanostructures for energy storage applications, *Appl. Phys. A: Mater. Sci. Process.*, 2023, **129**(1), 49.
37 S. Hussain, *et al.*, Unique hierarchical mesoporous LaCrO3 perovskite oxides for highly efficient electrochemical energy storage applications, *Ceram. Int.*, 2019, **45**(12), 15164–15170.
38 H. Li, *et al.*, Facile synthesis of mesoporous MnO2 microspheres for high performance AC//MnO2 aqueous hybrid supercapacitors, *Electrochim. Acta*, 2013, **108**, 497–505.
39 K. Shimamoto, K. Tadanaga and M. Tatsumisago, All-solid-state electrochemical capacitors using $MnO_2$/carbon nanotube composite electrode, *Electrochim. Acta*, 2013, **109**, 651–655.
40 H. Wang, *et al.*, Design, synthesis and the electrochemical performance of MnO2/C@ CNT as supercapacitor material, *Mater. Res. Bull.*, 2013, **48**(9), 3389–3393.

41 S. Zhao, *et al.*, Li-ion uptake and increase in interlayer spacing of Nb4C3 MXene, *Energy Storage Mater.*, 2017, **8**, 42–48.
42 G. Deysher, *et al.*, Synthesis of Mo4VAlC4 MAX phase and two-dimensional Mo4VC4 MXene with five atomic layers of transition metals, *ACS Nano*, 2019, **14**(1), 204–217.
43 G. Li, *et al.*, Highly efficient Nb2C MXene cathode catalyst with uniform O-terminated surface for lithium–oxygen batteries, *Adv. Energy Mater.*, 2021, **11**(1), 2002721.
44 N. Prabhakar, *et al.*, Effect on delamination of Nb4C3Tx MXene supported tungsten oxide for high-performance supercapacitor, *J. Energy Storage*, 2024, **98**, 112830.
45 P. Varatharajan, *et al.*, A wide linear range and highly sensitive electrochemical reduction of environmental hazard (p-Nitrotoluene) using carbon-based hybrid composite ($Ti_3C_2TX$@$MnCo_2O_4$), *J. Environ. Chem. Eng.*, 2024, **12**(6), 114301.
46 U. Rajaji, *et al.*, $MoS_2$ sphere/2D S-$Ti_3C_2$ MXene nanocatalysts on laser-induced graphene electrodes for hazardous aristolochic acid and roxarsone electrochemical detection, *ACS Appl. Nano Mater.*, 2022, **5**(3), 3252–3264.
47 K. Shi, Z. Chen and W. Sun, Controlling of Crystal Facets by Dysprosium-Modified WO3/Carbon Nanofibers Enhance the Flexible Supercapacitor Performance, *Small*, 2024, **20**(50), 2405769.
48 X. Li, *et al.*, Manganese dioxide nanosheets decorated on MXene (Ti3C2Tx) with enhanced performance for asymmetric supercapacitors, *Ceram. Int.*, 2021, **47**(9), 12211–12220.
49 R. Shafique, *et al.*, Investigations of 2D Ti3C2 (MXene)-$CoCr_2O_4$ nanocomposite as an efficient electrode material for electrochemical supercapacitors, *Int. J. Energy Res.*, 2022, **46**(5), 6689–6701.
50 Y. Wei, *et al.*, All pseudocapacitive MXene-MnO2 flexible asymmetric supercapacitor, *J. Energy Storage*, 2022, **45**, 103715.
51 S. A. Zahra, E. Ceesay and S. Rizwan, Zirconia-decorated V2CTx MXene electrodes for supercapacitors, *J. Energy Storage*, 2022, **55**, 105721.
52 E. Ceesay, *et al.*, Improved pseudocapacitor and water splitting in cobalt-anchored vanadium carbide MXene nanocomposite, *Int. J. Hydrogen Energy*, 2024, **56**, 140–146.
53 W. Zheng, *et al.*, MXene—Manganese oxides aqueous asymmetric supercapacitors with high mass loadings, high cell voltages and slow self-discharge, *Energy Storage Mater.*, 2021, **38**, 438–446.
54 K. O. Oyedotun, *et al.*, Electrochemical performance of two-dimensional $Ti_3C_2$-$Mn_3O_4$ nanocomposites and carbonized iron cations for hybrid supercapacitor electrodes, *Electrochim. Acta*, 2019, **301**, 487–499.
55 D. Ponnalagar, *et al.*, Recent progress in two-dimensional $Nb_2C$ MXene for applications in energy storage and conversion, *Mater. Des.*, 2023, **231**, 112046.
56 K. Wasnik, *et al.*, MXenes: Advances in the synthesis and application in supercapacitors and batteries, *J. Mater. Res.*, 2022, **37**(22), 3865–3889.
57 T. Tajiri, *et al.*, Magnetic properties and crystal structure of $DyMn_2O_5$ nanoparticles embedded in mesoporous silica, *Phys. Proc.*, 2015, **75**, 1181–1186.
58 S. Vadivel and P. Sujita, Construction of ternary structured $Dy_2O_3$ nanorods/carbon spheres/few layered Dy2WO6 nanohybrids for electrochemical supercapacitors, *J. Rare Earths*, 2024, DOI: **10.1016/j.jre.2024.09.005**.
59 H. P. Klug and L. E. Alexander, *X-ray diffraction procedures: for polycrystalline and amorphous materials*. 1974.
60 D. Hull and D. Bacon, *Introduction to Dislocations*, 5th edn, Butterworth, Heinemann, 2011.
61 M. C. Roco, C. A. Mirkin and M. C. Hersam, *Nanotechnology research directions for societal needs in 2020: retrospective and outlook*. 2011.
62 N. Arif, *et al.*, Synthesis and characterization of layered Nb2C MXene/ZnS nanocomposites for highly selective electrochemical sensing of dopamine, *Ceram. Int.*, 2021, **47**(2), 2388–2396.
63 L. Xue, *Study on Spectroscopy of Rare Earth Oxides and Mineral*. 2003.
64 G. V. Chertihin and L. Andrews, Reactions of laser-ablated manganese atoms with dioxygen. Infrared spectra of MnO, OMnO, Mn (O2),(MnO) 2, and higher oxide complexes in solid argon. The, *J. Phys. Chem. A*, 1997, **101**(45), 8547–8553.
65 B. J. Janani, *et al.*, Robust advantage of MXene/g-C3N4 loaded on Fe2WO6/BiIO4 nano-platform for chemo-peroxidase colorimetric detection of uranyl ions, antifungal properties, photocatalytic degradation of p-chlorophenol, and eco-toxicity studies, *Diamond Relat. Mater.*, 2024, **145**, 111129.
66 Fd. O. Cantão, *et al.*, Utilization of Sn/Nb2O5 composite for the removal of methylene blue, *Quim. Nova*, 2010, **33**, 528–531.
67 K. Gopinath, *et al.*, One-pot synthesis of dysprosium oxide nano-sheets: antimicrobial potential and cyotoxicity on A549 lung cancer cells, *J. Cluster Sci.*, 2017, **28**, 621–635.
68 Y. Cao, *et al.*, High-performance acetone gas sensor based on ferrite–$DyFeO_3$, *J. Mater. Sci.*, 2020, **55**, 16300–16310.
69 Jd. A. Pereira, *et al.*, Tuning the morphology of manganese oxide nanostructures for obtaining both high gravimetric and volumetric capacitance, *Mater. Adv.*, 2020, **1**(7), 2433–2442.
70 Z. Yang, *et al.*, XPS studies of nitrogen doping niobium used for accelerator applications, *Appl. Surf. Sci.*, 2018, **439**, 1119–1126.
71 M. A. Melo, *et al.*, Niobium-doped Hematite Photoanodes Prepared through Low-Cost Facile Methods for Photoelectrochemical Water Splitting, *ChemCatChem*, 2023, **15**(14), e202300387.
72 A. Kirakosyan, *et al.*, Poly (styrene sulfonic acid)-grafted carbon black synthesized by surface-initiated atom transfer radical polymerization, *Molecules*, 2023, **28**(10), 4168.
73 K. A. Rao, M. E. Mazhar and J. Ahmad, Facile hydrothermal synthesis of a tri-metallic Cu–Mn–Ni oxide-based electrochemical pseudo capacitor, *Dalton Trans.*, 2024, **53**(31), 13012–13021.

 

74 S. Kaipannan and S. Marappan, Fabrication of 9.6 V high-performance asymmetric supercapacitors stack based on nickel hexacyanoferrate-derived Ni (OH) 2 nanosheets and bio-derived activated carbon, *Sci. Rep.*, 2019, **9**(1), 1104.

75 A. Sami, *et al.*, Enhanced supercapacitor performance of rGO-Supported $BaVO_3$ nanostructures as advanced electrode materials, *Ceram. Int.*, 2025, **51**(7), 8480–8491.

76 B. Saravanakumar, *et al.*, Electrochemical properties of rice-like copper manganese oxide ($CuMn_2O_4$) nanoparticles for pseudocapacitor applications, *J. Alloys Compd.*, 2017, **723**, 115–122.

77 J. Wang, *et al.*, Pseudocapacitive contributions to electrochemical energy storage in TiO2 (anatase) nanoparticles, *J. Phys. Chem. C*, 2007, **111**(40), 14925–14931.

78 K. Kannadasan, *et al.*, Sea Urchin-Like NiO-CoO Heterostructure as High-Energy Supercapattery Electrode: Laboratory Prototype to Field Application of Pouch-type Device, *ACS Appl. Electron. Mater.*, 2024, **6**(7), 5269–5282.

79 N. K. Sakthivel, M. Govindasamy and P.-Y. Chen, Sonochemical Synthesis of Perovskite Embedded with Carbon Nanofibers as an Electrode Material for Energy Storage Application, *J. Electrochem. Soc.*, 2025, **172**(4), 040519.

80 R. Packiaraj, *et al.*, Electrochemical performances of ZnO–NiO–CuO mixed metal oxides as smart electrode material for solid-state asymmetric device fabrication, *Energy Fuels*, 2021, **36**(1), 603–617.

81 X. Zhang, *et al.*, Effect of aqueous electrolytes on the electrochemical behaviors of supercapacitors based on hierarchically porous carbons, *J. Power Sources*, 2012, **216**, 290–296.

82 J. Sun, *et al.*, Bundlelike $CuCo_2O_4$ microstructures assembled with ultrathin nanosheets as battery-type electrode materials for high-performance hybrid supercapacitors, *ACS Appl. Energy Mater.*, 2020, **3**(8), 8026–8037.

83 B. Subramanian, *et al.*, Synthesis and Characterization of $Dy_2O_3$@$TiO_2$ Nanocomposites for Enhanced Photocatalytic and Electrocatalytic Applications, *ACS Eng. Au*, 2024, **4**(5), 474–490.

84 R. Fang, *et al.*, 2 D MXene-based energy storage materials: interfacial structure design and functionalization, *ChemSusChem*, 2020, **13**(6), 1409–1419.

85 G. George, *et al.*, Effect of doping on the performance of high-crystalline $SrMnO_3$ perovskite nanofibers as a supercapacitor electrode, *Ceram. Int.*, 2018, **44**(17), 21982–21992.

86 S. Nagamuthu, S. Vijayakumar and K.-S. Ryu, Cerium oxide mixed LaMnO3 nanoparticles as the negative electrode for aqueous asymmetric supercapacitor devices, *Mater. Chem. Phys.*, 2017, **199**, 543–551.

87 P. Amalthi, *et al.*, Microwave-aided fabrication of calcium-substituted DyMnO3 nanocomposites as prospective battery-type electrode material for supercapacitors, *Mater. Sci. Eng. B*, 2023, **298**, 116845.

88 J. Singh, *et al.*, Mesoporous spheres of Dy 2 NiMnO 6 synthesized via hydrothermal route for structural, morphological, and electrochemical investigation, *Ionics*, 2020, **26**, 5143–5153.

89 J. Singh, U. K. Goutam and A. Kumar, Hydrothermal synthesis and electrochemical performance of nanostructured cobalt free $La_2CuMnO_6$, *Solid State Sci.*, 2019, **95**, 105927.

90 M. Alam, *et al.*, Electrochemical supercapacitor based on double perovskite $Y_2NiMnO_6$ nanowires, *RSC Adv.*, 2016, **6**(115), 114722.

91 D. Gangwar, *et al.*, Effect of Dy on electrochemical supercapacitive behaviour of α-MnO2 nanorods, *Electrochim. Acta*, 2019, **328**, 135027.

92 T. Brousse, *et al.*, Long-term cycling behavior of asymmetric activated carbon/MnO2 aqueous electrochemical supercapacitor, *J. Power Sources*, 2007, **173**(1), 633–641.

93 B. Safdar, *et al.*, Self-standing star-shaped tri-metallic oxides for pseudocapacitive energy storage electrode materials, *Appl. Surf. Sci.*, 2020, **530**, 147251.

94 L. Li, *et al.*, Facile synthesis of MnO2/CNTs composite for supercapacitor electrodes with long cycle stability. The, *J. Phys. Chem. C*, 2014, **118**(40), 22865–22872.

95 C. K. Kamaja, *et al.*, Effect of Aqueous Electrolytes on the Performance of a Ti3C2T x (MXene)– δ-MnO2 Asymmetric Supercapacitor, *Energy Fuels*, 2021, **36**(1), 703–709.

96 B. T. Vetrikarasan, *et al.*, Co-precipitation synthesis of pseudocapacitive λ-$MnO_2$ for 2D MXene (Ti3C2Tx) based asymmetric flexible supercapacitor, *J. Energy Storage*, 2023, **72**, 108403.

97 I. Ashraf, *et al.*, Ni-doped CeO2 decorated delaminated layered titanium carbonitride (d-Ti3CN) MXene for potential applications in symmetric supercapacitors, *J. Alloys Compd.*, 2023, **952**, 170043.

98 M. Sharma, *et al.*, Combustion synthesis, structural and electrochemical studies on the dysprosium-doped cobalt ferrite nanoparticles to investigate its performance as a supercapacitor electrode, *Mater. Chem. Phys.*, 2024, **324**, 129676.